REVIEW

Promises and challenges of perovskite solar cells

Juan-Pablo Correa-Baena,[1,2]* Michael Saliba,[2] Tonio Buonassisi,[1] Michael Grätzel,[2] Antonio Abate,[3] Wolfgang Tress,[2] Anders Hagfeldt[2]*

The efficiencies of perovskite solar cells have gone from single digits to a certified 22.1% in a few years' time. At this stage of their development, the key issues concern how to achieve further improvements in efficiency and long-term stability. We review recent developments in the quest to improve the current state of the art. Because photocurrents are near the theoretical maximum, our focus is on efforts to increase open-circuit voltage by means of improving charge-selective contacts and charge carrier lifetimes in perovskites via processes such as ion tailoring. The challenges associated with long-term perovskite solar cell device stability include the role of testing protocols, ionic movement affecting performance metrics over extended periods of time, and determination of the best ways to counteract degradation mechanisms.

Photovoltaic (PV) devices convert solar energy into electricity and are promising candidates to offset carbon emissions while providing an alternative way to meet increasing demand in energy consumption. Several PV technologies have helped to shape the environment of renewable sources of energy (*1*). High-purity crystalline silicon has achieved power conversion efficiencies (PCEs) exceeding 26% (*2*) and long-term durability, making it an ideal product for the market. However, emerging PV technologies based on thin films (<1 μm) and simple deposition methods promise to reduce production cost and produce high-quality semiconductors for solar cells, rivaling other established ones such as Si, CdTe, and GaAs (*3*, *4*). Lead halide perovskite solar cells (PSCs) have emerged as one such candidate. In just a few years, PSCs have achieved PCEs similar to those of established CdTe solar cells, surpassing the 22% mark in 2016 (*5*).

Despite impressively high efficiencies, PSCs face challenges such as long-term durability that prevent them from competing with established technologies. However, advancements in materials processing during the past 2 years have yielded remarkable progress in long-term material and device stability, enabling the research community to better identify intrinsic versus extrinsic degradation mechanisms, some of which are summarized here. Despite the rapid improvement in performance, there is still room for tailoring charge carrier recombination, both in the perovskite and at the interfaces within the device, to increase PCEs. Major challenges to long-term stability also remain.

Device configurations

Lead halide perovskites can adopt an ABX_3 structure, where the A site is typically composed of organic methylammonium (MA), formamidinium (FA), or inorganic Cs or Rb cations. The Pb sits in the B site; the X site is occupied by the halides I, Br, or Cl. These are the most widely studied compounds yielding high performance metrics in PV devices. The configuration of PSCs has not changed substantially since the first solid-state devices were introduced in 2012 (*6*, *7*). In general, a transparent conducting glass serves as the substrate where an electron-selective (n-i-p configuration) or hole-selective (p-i-n configuration) contact is deposited, followed by the perovskite absorbing layer, and topped by the hole- or electron-selective layer and a metal contact (Fig. 1, A to C). More recently, multijunction PV devices (tandems) (*8*, *9*), where two band gap–matched absorbers are monolithically stacked, have shown promise for their low cost and potential to exceed the single-junction Shockley-Queisser efficiency limit (Fig. 1D) (*10*).

> ***"...long-term stability is still one of the key issues that impedes rapid commercialization..."***

Mesostructured devices (Fig. 1A), based on thick alumina and titania nanoparticle films infiltrated with a perovskite material [e.g., methylammonium lead triiodide ($MAPbI_3$)], were initially the most efficient (*11*, *12*). Starting in 2014, the mesostructured film thickness was decreased to 200 nm; this film, topped by a 200-nm perovskite layer (Fig. 1A), yielded certified PCEs above 16% (*13*). This compact perovskite layer was subsequently optimized to 500 nm to provide even greater light harvesting (*14*). Mesoporous PSCs typically require a high-temperature sintering step, which excludes the use of plastics with low melting points as support materials. A simplified, often low-temperature, alternative omits the mesoporous layer and is referred to either as a planar n-i-p (Fig. 1B) or planar p-i-n (Fig. 1C) PSC, depending on the sequence of charge-selective layers. For the former, the stack order is a transparent conducting oxide, such as fluorine-doped tin oxide (FTO)/electron-selective layer/perovskite/hole-selective layer/metal configuration, whereas for the latter, the contacts are flipped.

For monolithically integrated all-perovskite tandems, both individual cells must be arranged as n-i-p or p-i-n. Because it is challenging to find orthogonal solvents for the subsequent deposition of the two perovskite films, vacuum processing is an attractive approach for making all-perovskite tandems (*15*). Alternatively, indium tin oxide (ITO) can be sputtered as a conducting protective layer to avoid damaging the perovskite film of the bottom cell during the solution-based deposition of the subsequent perovskite (*10*).

State-of-the-art devices

Efficiencies in PSCs have risen quickly since their introduction in 2009 (*16*), but PCEs of >20% were reported only in 2015 (*17*), with a few others reported thereafter (Fig. 1E) (*18*–*25*). These results have been achieved by tailoring the proportions of MA, FA, I, and Br to improve electronic properties. A stabilized efficiency of 21.6% was reported (*21*) with a 200-nm mesoporous TiO_2 layer that uses a 500-nm perovskite layer composed of Rb, Cs, MA, and FA as the cations, Pb as the B-site cation, and I and Br as the X-site anion. A PSC with a similar device configuration achieved a certified PCE of 22.1% (highest reported) by iodide addition, which was shown to decrease the concentration of deep-level traps (*25*). Si/perovskite monolithic tandems with efficiencies up to 23.6% have been achieved by optimizing the interfaces and the band gap of the perovskite top cell (*26*). Perovskite-perovskite monolithic tandems have been achieved with efficiencies of 17% (*10*) and 18% (*15*) via solution processing and vacuum deposition, respectively.

In terms of device metrics, short-circuit currents (J_{SC}) have been maximized (Fig. 1E), with most state-of-the-art devices yielding numbers near the theoretical and practical maxima (*14*). Similarly, fill factors (FF) have been maximized (Fig. 1E) for the open-circuit voltage (V_{OC}) that these devices achieve. In addition, as V_{OC} is increased, so is FF. Thus, in order to surpass 22.1% efficiency (*25*), efforts need to be made to improve V_{OC} and FF. This goal requires identifying and suppressing recombination pathways to boost these crucial PV parameters (*27*, *28*).

All of the certified PCEs greater than 20% have been measured with a small area of illumination (roughly 0.2 to 0.1 cm^2). Measuring devices over a larger area (>1 cm^2) is more meaningful for upscaling efforts. However, spin coating—the main method used to achieve all recent efficiency records—tends to produce nonuniform layers over larger areas, and measurements over such large areas may therefore be inaccurate. In addition, the device configuration must be changed to ensure minimized distance (and thus resistance) for charges traveling to the electrodes. Nonetheless,

[1]Massachusetts Institute of Technology, Cambridge, MA 02139, USA. [2]École Polytechnique Fédérale de Lausanne, CH-1015 Lausanne, Switzerland. [3]Helmholtz-Zentrum Berlin für Materialien und Energie, 12489 Berlin, Germany.
*Corresponding author. Email: jpcorrea@mit.edu (J.-P.C.-B.); anders.hagfeldt@epfl.ch (A.H.)

even with spin coating, efficiencies up to 19.7% have been achieved on areas larger than 1 cm^2 (*25*, *29*). More work in deposition (e.g., printing or vacuum-processed PSCs) and device optimization is needed to achieve large-area, upscalable PSCs with efficiencies of >20%.

Device photophysics

PSCs are heterojunction devices in which the hole-selective or electron-selective contacts (or both) introduce the selectivity required to harvest charge carriers at their respective electrodes to create a photovoltage. After an initial period of controversy, consensus has been reached that these interfaces are not required to dissociate a photogenerated electron-hole pair (exciton), because the exciton binding energy is comparable (some tens of millielectron volts) (*30*) to the thermal energy under operation. This property, paired with a relatively large diffusion length (*31*) and sufficiently high mobilities of electrons and holes (*32*), allowed for high internal quantum efficiencies even for the first reported PSCs. The absorption coefficient itself, shown in Fig. 2A, is high (>10^5 cm^{-1}) because of a direct transition at the band gap. One of the device optimization steps toward higher efficiency was to increase the thickness of the perovskite layer to reach a sharp onset of the external quantum efficiency (EQE) near the band gap, which is ~1.6 eV for the most efficient MAFA-based compounds. The photocurrent of the device shown in Fig. 2A (*14*), 23 mA cm^{-2}, is rather optimized and could only be slightly increased (by 1 to 2 mA cm^{-2}) in the case of a sharper EQE onset at 780 nm.

Nominally, most of the perovskite architectures look like a metal(-like)/electron-selective layer/intrinsic perovskite/p-type hole conductor system (Fig. 1, A to C). The work function difference of the electrodes including doped charge transport layers could introduce a built-in potential generating an electric field in the perovskite film in equilibrium, or the perovskite itself could be either n- or p-doped depending on its stoichiometry (*33*) and forming a p-n junction somewhere in the device. Varying results have been reported on the energetics of perovskites, such as a work function located far in the conduction band and ionization energies that depend on the stoichiometry (*34*).

The electric field distribution is further influenced by intrinsic defects induced by movement of ions, such as I. These tend to screen the electric field by accumulating at interfaces, similar to mobile ions in an electrolyte. Low mobilities cause ionic defects to respond slowly (seconds to minutes) to voltage changes and are believed to be responsible for the frequently observed hysteresis in the current-voltage curve (Fig. 2B) (*35*–*37*). The hysteresis reflects that the collection efficiency of photogenerated charge carriers is dependent on the biasing history and on the electric field. Thus, hysteresis can be minimized by either immobilizing ionic charge or increasing charge carrier transport and extraction to make the latter less sensitive to the electric field (*38*). Here, charge extraction layers, trap densities at the interfaces, and the morphology of the perovskite are influential.

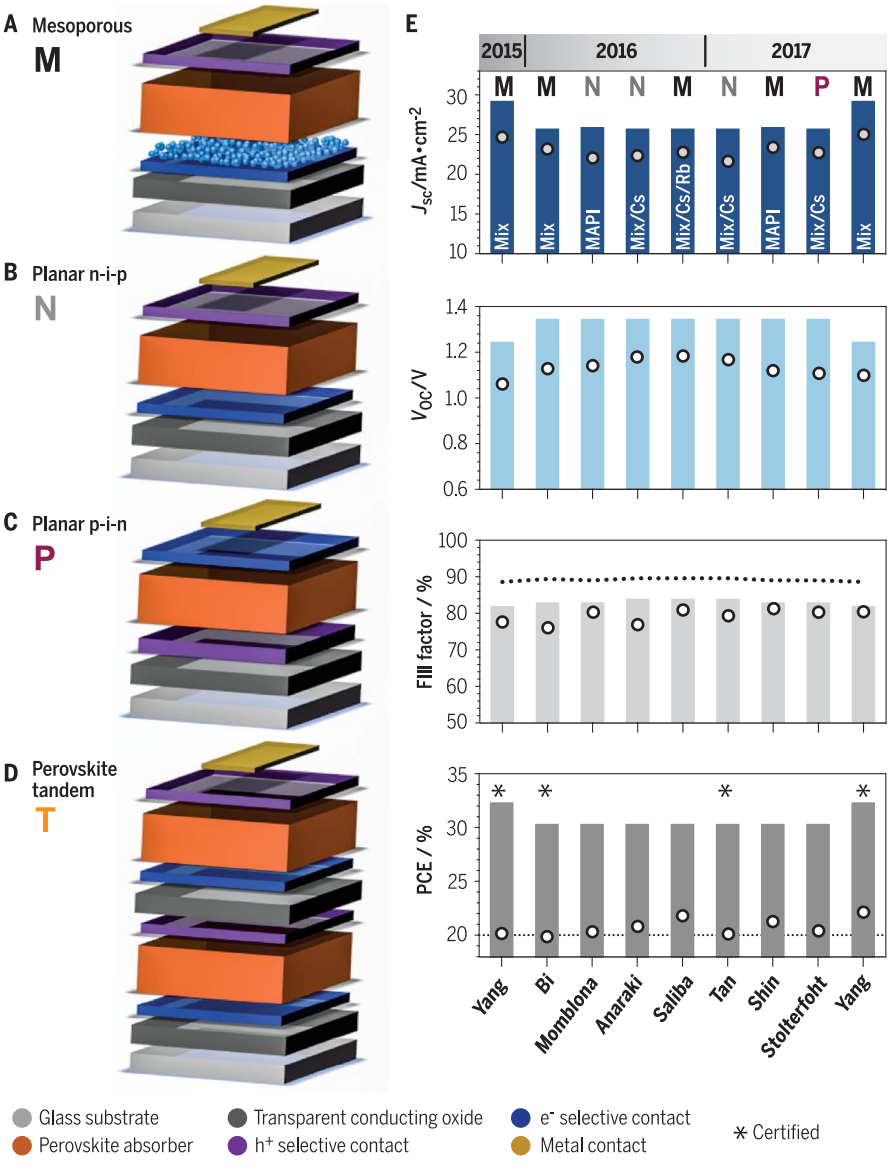

Fig. 1. Commonly used PSC architectures and their state-of-the-art performance. (**A** and **B**) Schematics of perovskite solar cells based on a mesoporous layer (A) and planar n-i-p (B), with a conducting glass/electron contact/perovskite configuration. (**C**) The p-i-n configuration with a planar junction in a conducting glass/hole contact/perovskite stack, also commonly referred to as "inverted." (**D**) Multijunction perovskite tandem where two or more band gap–matched absorbers are stacked to increase overall PCE. (**E**) Photovoltaic parameters of PSCs as calculated from the Shockley-Queisser model (bars) and metrics of selected publications (circles) with efficiencies above 20% since 2015 and in chronological order to 2017 (*17*–*25*). The calculated fill factor has two maxima: (i) the maximum for the measured V_{OC} (bars) assuming Shockley-Read-Hall recombination, and (ii) the maximum under the assumption that the theoretical V_{OC} is achieved (dotted line). See supplementary materials for details of the calculations. Configurations: M, mesoporous; N, planar n-i-p; P, planar p-i-n; T, perovskite tandem. The perovskite composition for each report is marked in the top panel, where "mix" refers to a combination of lead-based FA, MA, I, and Br ions. Inorganic cations Rb and Cs are used in some recipes; MAPI, methylammonium lead triiodide.

Recombination

Charges that are not collected are lost by recombination. Open-circuit conditions are ideal for studying recombination processes because no photogenerated charges are extracted. The very high V_{OC} of PSCs relative to the perovskite band gap is indicative of low recombination losses. Deposition, composition, and device engineering have increased V_{OC} to values as high as 1.24 V at a band gap of ~1.6 eV (*21*). An ideal

absorber material of that band gap could deliver a V_{OC} of 1.33 V (*39*). In a real device, bulk defects, surfaces, and interfaces introduce recombination centers that lead to fast nonradiative losses. Thus, long-lived charges are desired and indeed are observed in transient photoluminescence experiments, where decay times in the range of several hundreds of nanoseconds (*18*) or even microseconds (*21*, *40*) have been reported.

These values are higher than lifetimes in GaAs (tens of nanoseconds) but lower than those in Si (tens of milliseconds) (*28*). Because lifetime can often be difficult to interpret, we prefer steady-state luminescence quantum yield, which can be determined by, for example, an electroluminescence measurement (*39*). A high radiative (band-to-band) recombination rate is beneficial for a high V_{OC} and for a large absorption coefficient because of the reciprocity between absorption and emission. Although the radiative rate constant is a material property, the nonradiative lifetime is commonly dominated by defect recombination. Calculating how a constant nonradiative lifetime influences V_{OC} (Fig. 2C) shows that increasing the nonradiative lifetime toward 10 μs is sufficient to reach the ultimate V_{OC}. In this case, the maximum FF, which is also limited by recombination, would approach 90%.

An additional loss mechanism is surface recombination, where charges are lost at the "wrong" electrode. Disentangling bulk and surface recombination in an ambipolar, nominally intrinsic thin semiconductor film between electrodes is challenging. Recently, it was reported that the PEDOT:PSS [poly(3,4-ethylenedioxythiophene) polystyrene sulfonate] electrode constitutes a large source of surface recombination in planar p-i-n PSCs (*41*), and dopants in the hole contact can be problematic in the planar n-i-p and mesoporous configurations (*27*). However, the planar SnO_2 (*42*) and mesoporous TiO_2 contacts in the n-i-p device configuration do not seem to dominate recombination, as long as they are deposited conformally (*27*). The role of grain boundaries on recombination in the perovskite film is still under debate (*27*, *43*). Impurities in the precursor material could be a further source of defects (*44*). Most of the intrinsic point defects are not expected to act as recombination centers, as they form shallow states (*45*, *46*) because of the unconventional antibonding nature of the valence states. Perovskites are therefore said to be defect-tolerant, explaining why a solution-processed material from precursors of chemical-grade purity can reach such low losses in potential [V_{OC} – (band gap/elementary charge)].

The loss in potential is the main property that influences how close a solar cell material can approach its thermodynamic, or Shockley-Queisser, limit. Figure 2D shows that a band gap between 1.1 and 1.4 eV is ideal to best harvest the energy of the solar spectrum. Thus, band gap tuning—for example, by mixing halides or making Sn-Pb compounds (Fig. 2, D and E)—is one of the main approaches for improving efficiency. To date, the efficiencies of the modified band gap materials (below 1.4 eV) are not yet near their Shockley-Queisser limit, mainly because of a greater loss in potential of the unoptimized devices based on Sn^{2+}, which can easily oxidize to Sn^{4+}. Similarly, for perovskites with wider band gaps, iodine and bromine mixing can lead to segregation of the individual components (*47*, *48*), forming undesired recombination centers and therefore a large loss in potential.

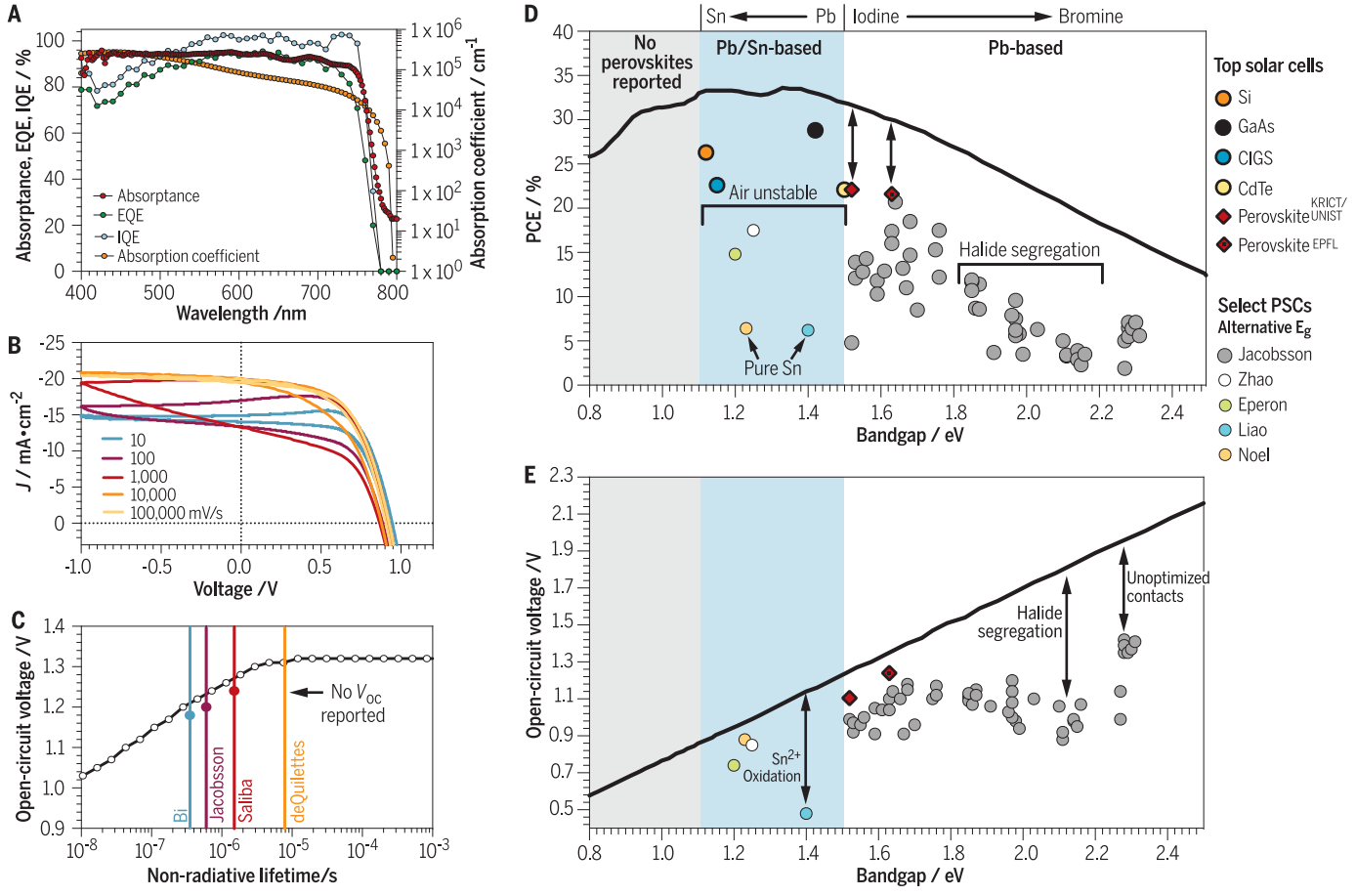

Fig. 2. Device photophysics of state-of-the-art PSCs. (**A**) Light-harvesting efficiency (absorptance), external and internal quantum efficiency (EQE and IQE), and absorption coefficient of a mixed ion-based PSC (*14*). (**B**) Current-voltage hysteresis under 1-sun illumination (*37*). (**C**) Calculation of the maximum V_{OC} as a function of nonradiative lifetime for a perovskite layer 500 nm thick, compared with values achieved by Bi *et al*. (*18*), Jacobsson *et al*. (*48*), Saliba *et al*. (*21*), and deQuilettes *et al*. (*40*). See supplementary materials for details of the calculations. (**D** and **E**) Shockley-Queisser efficiency (D) and calculated maximum V_{OC} (radiative limit) (E) for a select number of PSCs by Jacobsson *et al*. (*48*), Zhao *et al*. (*58*), Eperon *et al*. (*10*), Liao *et al*. (*81*), and Noel *et al*. (*82*), compared with different established solar cells.

Perovskite material instability and halide segregation

The optical properties of perovskite materials can be tuned when the halides (X site in the ABX_3 structure) are modified. For instance, increasing the Br content in an I perovskite increases the band gap toward 1.7 eV, which is highly desired for perovskite/silicon tandems (*49*). However, halide segregation with distinct Br and I domains occurs in single-cation MA-perovskites where Br and I are nearly equimolar (*47*). Not only is such dephasing problematic because it can promote recombination centers, it can also affect the long-term stability of materials. Perovskites with MA cations have raised concerns regarding stability because of their volatile nature at temperatures as low as 85°C, and they have been shown to degrade readily upon exposure to moisture and heat (*50*). Recent reports have shown, however, that $MAPbI_3$ perovskites are not susceptible to light soaking (*23*).

Cations enable perovskite black-phase stabilization

Because FA is more thermally stable and the band gap of $FAPbI_3$ is narrower than that of $MAPbI_3$ (*51*, *52*), FA-based perovskites have recently become a major avenue of research, promising higher theoretical efficiency limits (Fig. 2D). However, these FA compounds tend not to form the photoactive "black" perovskite phase at room temperature but exhibit a photoinactive "yellow" phase (*53*, *54*), in particular when mixing Br and I for wider band gaps. This "yellow-phase gap" was closed by using double-cation CsFA mixtures (*49*, *52*, *55*, *56*). The resulting materials also suppressed halide segregation (*49*). On the other hand, some of the highest performance metrics are achieved with complex perovskite mixtures containing some combination of multiple cations (including Rb, Cs, MA, and FA), metals (Pb and Sn), and halides (Br and I). For example, a stabilized PCE of 21.6% with improved reproducibility (Fig. 3A) was reached using a multication mixture of Rb, Cs, MA, and FA together with mixed Br and I halides (*10*, *57*, *58*). This result is part of a broader theme of efforts aimed at phase stabilization and suppressed halide segregation of perovskites through multication engineering (*21*).

There are only a limited number of A cations in an $APbI_3$ perovskite that support a photoactive black phase. One empirical measure for lattice distortion is the Goldschmidt tolerance factor (t) that was found to be between 0.8 and 1.0 for black-phase perovskites (Fig. 3B) (*59*). Only Cs, MA, and FA fall within the "established" category of perovskites, and other cations are too small (see Na, K, Rb) or too large (imidazolium, ethylamine, and guanidinium) for consideration. Perovskites at the edge of the tolerance factor requirement, such as $FAPbI_3$ ($t \sim 1$) and $CsPbI_3$ ($t \sim 0.8$), have a distorted lattice resulting in the presence of a yellow phase at room temperature. In contrast, $MAPbI_3$ ($t \sim 0.9$) does not have a yellow phase.

To lower the effective cationic radius of FA-based perovskites, MAFA perovskites were created by adding the smaller MA cation. This material had a more stable black phase at room temperature, triggering a remarkable success story; most currently published world record efficiencies were achieved using MAFA mixtures (Fig. 1E) (*17*, *25*, *60*). Interestingly, the x-ray diffraction (XRD) data of MAFA often show detrimental yellow-phase impurities (*61*); hence, adding small amounts of Cs to MAFA compositions was posited to reduce the yellow-phase impurities. Indeed, the CsMAFA triple-cation perovskite showed substantially suppressed yellow-phase impurities (*61*).

This finding becomes particularly noteworthy when analyzing the XRD data of films without annealing. For MAFA, multiple crystalline precursor states exist, whereas for CsMAFA, a well-defined perovskite peak emerges. Thus, the perovskite crystallization starts with the photoactive black phase, and indeed, triple-cation perovskites processed only at room temperature can achieve PCEs of 18%, whereas unannealed MAFA perovskite analogs are barely functional (*62*). These underappreciated variables, such as processing temperature and humidity, are likely the main reason why so many groups struggled to reproduce results with seemingly the same procedures and protocols. CsMAFA perovskites have increased the performance baseline, and the often overlooked parameter of reproducibility was improved, as evidenced by many subsequent studies with this material and ones of similar composition (*22*, *61*, *63*). In our laboratory, we were only able to pinpoint these critical variables by working with large batch sizes and meticulous recording of all results, including materials with poor PCEs, and we note that providing statistically relevant data is of utmost relevance for the future direction of the field (Fig. 3A).

Recently, the seemingly too small Rb was used in a multication approach despite $RbPbI_3$ not forming a black-phase single-cation perovskite. Rb-modified perovskite compositions including RbFA, RbMAFA, RbCsFA, and RbCsMAFA provide an additional avenue for prospective materials (*21*). Analogously to Rb, a doubling of available compounds could be achieved by identifying an additional cation, but currently there are no further cations that have been demonstrated for PSCs beyond 20% efficiency. Looking at the tolerance factor in Fig. 3B, there are two possible directions: selecting smaller cations than Rb (e.g., alkali metals such as Na and K) or selecting larger cations than FA (e.g., imidazolium, ethylamine, and guanidinium) (see Fig. 3B for structures). Thus far, K can integrate into a Cs-based perovskite, which, however, has a suboptimal band gap toward 2 eV (*64*). Sodium has been investigated as well, but thus far no integration has been clearly demonstrated (*65*). Adding larger molecules to 3D perovskites (where the metal-halide octahedra are interconnected) frequently results in 2D-3D perovskites where the metal layers are separated by the larger cations (*66*, *67*). These compounds are promising but are still trailing in terms of overall performance. However, the multication approach yielded some of the most stable and efficient devices so far.

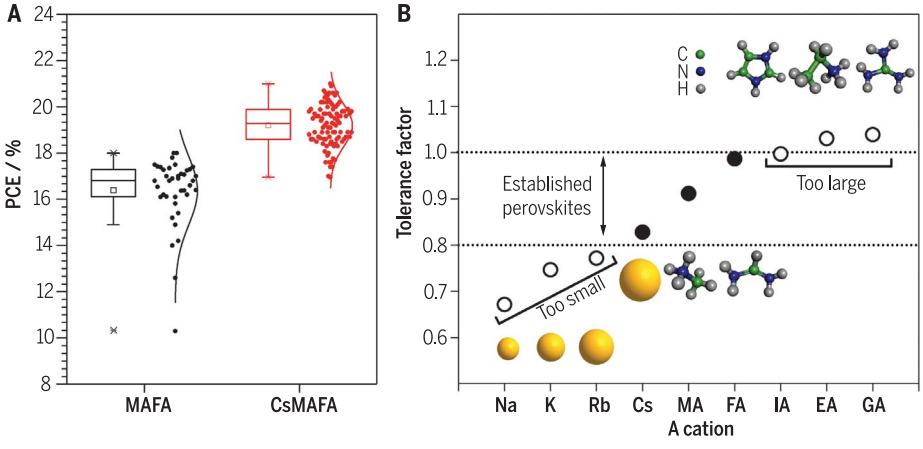

Fig. 3. The role of cations in the reproducibility of highly efficient perovskite solar cells. (**A**) Comparison of PCE values, with box plots shown alongside the corresponding data points, between 40 MAFA double-cation and 98 CsMAFA triple-cation perovskite devices. The standard deviation, a metric for reproducibility, improved from 16.37 ± 1.49% for MAFA to 19.20 ± 0.91% for CsMAFA. Twenty independent devices showed efficiencies larger than 20% (*61*). (**B**) Tolerance factor of $APbI_3$ perovskite with A cations that are too small (Na, K, Rb), established (Cs, MA, FA), or too large [imidazolium (IA), ethylamine (EA), guanidinium (GA)]. The inset images depict the cation structures. Empirically, perovskites with a tolerance factor between 0.8 and 1.0 (dotted lines) show a photoactive black phase (solid circles) as opposed to nonphotoactive phases (open circles). Rb is very close to this limit, making it a candidate for modification of the perovskite lattice via a multication approach (*21*).

PSC stability under working conditions

For the PV industry, the factors determining cost per kWh by a new solar technology are PCE and long-term stability. The PCE degradation over time controls the return on investment and thus

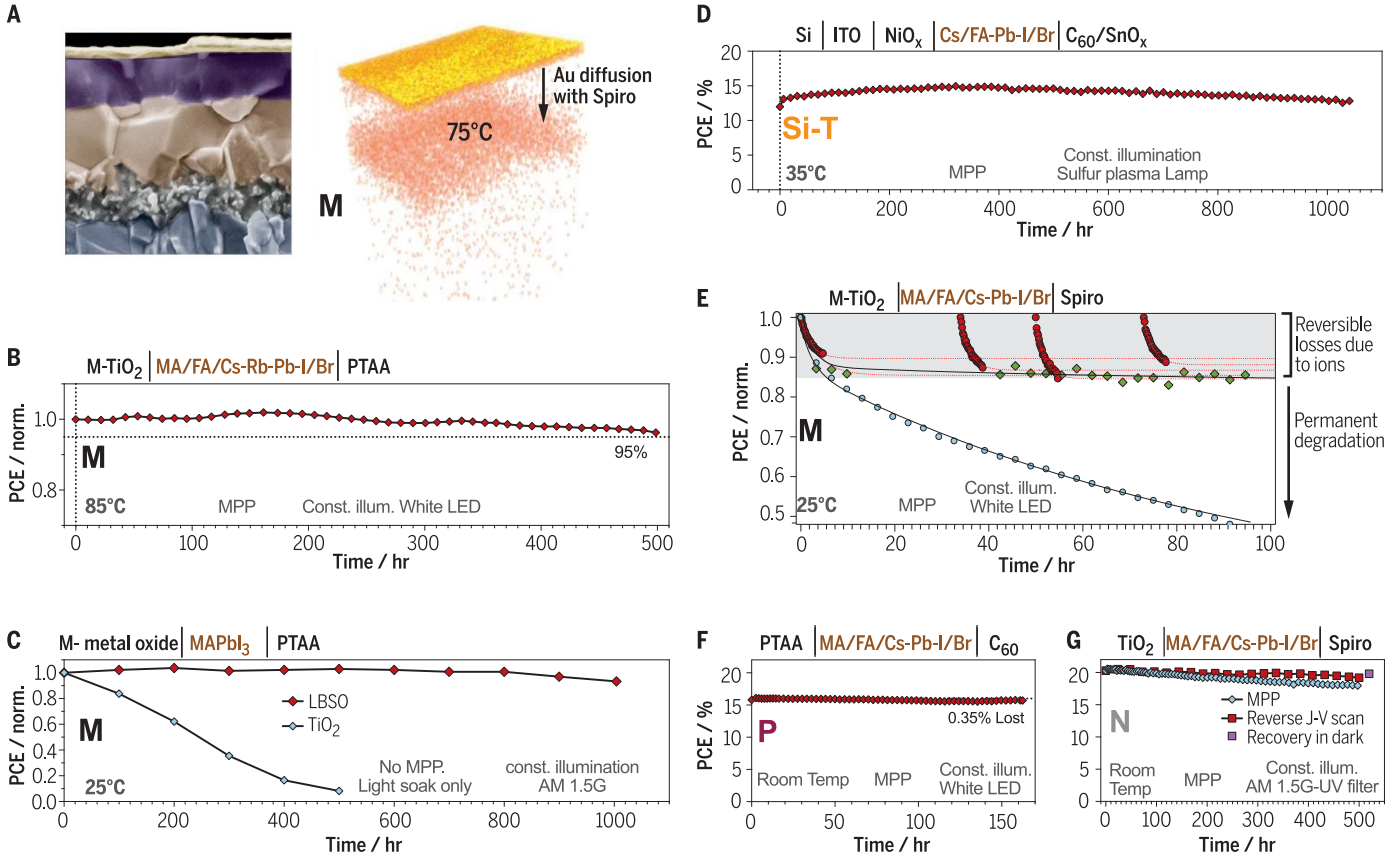

Fig. 4. Long-term stability of perovskite solar cells. (**A**) Gold migration through spiro-OMeTAD under light, MPPT, nitrogen flow at 75°C. [Adapted from (*69*) with permission] (**B**) The use of multiple cations and a PTAA hole contact shows losses of ~5% in 500 hours of MPPT in nitrogen at 85°C (*21*). (**C**) Photostability test under AM 1.5G illumination, including UV radiation for encapsulated devices based on different metal oxides (*23*). (**D**) Unencapsulated Si-perovskite tandems show remarkable MPPT stability, with a slight increase in performance and an almost unchanged performance at the end of the >1000-hour test (*26*). (**E**) MPPT of devices showing reversible losses before going through permanent degradation (*78*). (**F** and **G**) Room-temperature test with light soaking of planar p-i-n for 150 hours (*24*) (F) and light soaking of n-i-p for 500 hours (*22*) (G); the devices exhibit small losses under MPPT. Configurations: M, mesoporous; N, planar n-i-p; P, planar p-i-n; Si-T, Si-perovskite tandem. The layer compositions of the device stacks are summarized at the top of each graph. Each graph includes a summary of the aging conditions used.

the risks associated with a new PV technology. Thus, it is important to accurately predict the time dependence of the PCE. The market reference is crystalline silicon solar cells with an average degradation rate of 0.5% per year, which is often ensured for 25 years under operational conditions. To compete within the PV market, PSCs must reach similar levels of stability (e.g., 0.25 to 0.5% losses per year).

Extrinsic degradation factors

Before investigating the stability of perovskite materials, it is important to understand external factors that may enhance degradation in PSCs, which tends to be irreversible. One of the main degradation pathways has been linked to high-temperature device testing (above 60°C) or devices heated up by constant illumination. Until recently, it was believed that the MA cation is thermally unstable in the perovskite and is solely responsible for degradation. Several studies have now shown that spiro-OMeTAD [2,2′,7,7′-tetrakis (*N*,*N*-di-p-methoxyphenyl-amine)9,9′-spirobifluorene] crystallizes under thermal stress, which then creates pathways that allow for an interaction of the metal electrode and the perovskite (Fig. 4A) (*21*, *68*–*70*). The use of carbon electrodes has helped to alleviate this issue because these materials are thermally stable and do not seem to interact with the perovskite layer (*71*–*73*). Layers of a polymeric hole conductor such as polytriarylamine (PTAA) are robust to temperatures up to 85°C, and devices have been shown to maintain 95% of their efficiency after 500 hours at continuous maximum power point tracking (MPPT) and light soaking (Fig. 4B).

Other extrinsic degradation factors have been ascribed to hole conductor dopant migration, such as lithium salts migrating through the perovskite layer affecting the efficiency of devices (*74*). Ultraviolet (UV) light, present in the full solar spectrum, has been reported to be detrimental to the long-term stability of perovskites as it is absorbed by the electron-selective contact, TiO_2, initiating a chemical degradation (*75*). To partially circumvent this issue, electron-selective contacts with wide band gaps have been developed, offering superior UV stability relative to TiO_2 (Fig. 4C) (*23*, *75*, *76*). Alternatively, when using TiO_2, UV filters can be easily applied, offsetting this effect. For instance, with a coating of UV fluorophores, UV photons are downconverted to visible photons, boosting the photocurrent and filtering out UV photons (*77*); therefore, UV stability seems not to be the main concern in the quest for stability.

Analogous to organic PVs, the stability of perovskite solar cells is severely influenced by moisture. Proper encapsulation with the elastomeric polymer ethylene-vinyl acetate has been demonstrated to protect the PSCs against moisture and heat in the commonly used damp heat testing (*26*). Promising long-term stability results have been reported for unencapsulated Si-perovskite tandems (Fig. 4D) (*26*) and single junctions (*70*), topped by an ITO electrode that acts as a barrier to moisture. Other simple encapsulation schemes involving polymers have been successfully used. Polymer-coated devices tested on a roof withstood rain and variable temperature conditions for more than 90 days, showing no sign of degradation (*77*).

Intrinsic degradation factors: Ionic movement

Once environmental (e.g., moisture or UV) and other external factors (e.g., thermally unstable spiro-OMeTAD) have been addressed, intrinsic factors associated with the perovskite can be more properly assessed. Ionic movement in perovskites has been shown to lead to fast (seconds to minutes; Fig. 2B) and slow (minutes to hours; Fig. 4E) performance degradation, namely hysteresis (*37*) and reversible losses (*78*, *79*), respectively. In the latter, devices suffer from decreased PCE during aging and recover to the initial value after dark storage for a few hours. The reversible losses have been attributed to lattice deformation, and hence to halide migration within the perovskite, when the device warms up as a result of the infrared component of the sunlight (*79*). Alternatively, the losses have been assigned to migration of cations at a slower rate than halides (Fig. 4E) (*78*). A comprehensive study investigating the reversible losses on different device architectures prepared with different charge-selective contacts is still lacking. From the few studies reported, migration of ions within the perovskite seems to have a milder impact on the device performance for planar p-i-n (Fig. 4F) (*24*, *26*, *70*). Regardless, it is important to establish how organic and inorganic contacts affect the accumulation of ions at interfaces in the long term, because mild reversible losses might be an obstacle for long-term stability.

Shelf versus maximum power point stability

Long-term stability can be assessed in various ways, including storing devices on a shelf in the dark ("shelf test," Fig. 4C), MPPT in a controlled lab environment, and outdoor tests. The stress by intrinsic and extrinsic degradation parameters (illumination, voltage, current, temperature, atmosphere) varies considerably among these tests. Therefore, depending on how the devices are measured, different performance metrics can be extracted. For instance, stability curves (PCE versus time) can seem substantially better when extracted from periodically collected current-voltage curves (because of hysteresis) rather than continuous MPPT (Fig. 4G) (*11*, *22*). Establishing a robust protocol to measure operational long-term stability may require the adoption of conventional MPPT (rather than the shelf test) for perovskite-specific phenomena to simulate conditions closer to field operation.

Opportunities and challenges

PSCs have made remarkable advances in just a few years, in part by borrowing expertise from other more established fields, such as organic or dye-sensitized solar cells, for contact layers and architectures. Perovskites keep surprising with new applications such as x-ray detection, and have displayed impressive new properties such as long-lived hot carriers, which promise to allow exceeding the Shockley-Queisser limit in PSCs (*80*). The remarkably low loss in potential recently reported by PSCs (*21*) shows that this solution-processed solar cell could soon approach other state-of-the-art technologies, such as Si or GaAs.

Now that efficiencies are beyond 20%, the perovskite community must focus on long-term stability. More robust testing procedures are needed to properly assess PSC stability. MPPT under light soaking and high temperatures and humidity is warranted, as is, for instance, outdoor field testing in order to correlate accelerated indoor testing to real working conditions. Accelerated testing procedures designed in the past for Si or organic PV are currently being applied to PSCs. However, it is likely that some of these testing conditions are either too strict or too mild to give a current estimation of how the PCE will degrade with time, and therefore they need to be revisited by the community. Regardless, long-term stability is still one of the key issues that impedes rapid commercialization of PSCs and draws skepticism from established solar cell technologies. To become a player in the power market, PSCs must be able to last for at least 20 years with minimal degradation; in order to do so, both intrinsic and extrinsic degradation in the perovskite device stack must be offset.

REFERENCES AND NOTES

1. A. Polman, M. Knight, E. C. Garnett, B. Ehrler, W. C. Sinke, *Science* **352**, aad4424 (2016).
2. K. Yoshikawa *et al.*, *Nat. Energy* **2**, 17032 (2017).
3. D. B. Needleman *et al.*, *Energy Environ. Sci.* **9**, 2122–2129 (2016).
4. Z. Song *et al.*, *Energy Environ. Sci.* **10**, 1297–1305 (2017).
5. National Center for Photovoltaics (NCPV), National Renewable Energy Laboratory (NREL); www.nrel.gov/ncpv.
6. H.-S. Kim *et al.*, *Sci. Rep.* **2**, 591 (2012).
7. M. M. Lee, J. Teuscher, T. Miyasaka, T. N. Murakami, H. J. Snaith, *Science* **338**, 643–647 (2012).
8. J. P. Mailoa *et al.*, *Appl. Phys. Lett.* **106**, 121105 (2015).
9. S. Albrecht *et al.*, *Energy Environ. Sci.* **9**, 81–88 (2016).
10. G. E. Eperon *et al.*, *Science* **354**, 861–865 (2016).
11. J.-P. Correa-Baena *et al.*, *Energy Environ. Sci.* **10**, 710–727 (2017).
12. M. Saliba, J.-P. Correa-Baena, M. Graetzel, A. Hagfeldt, A. Abate, *Angew. Chem. Int. Ed.* 10.1002/anie.201703226 (2017).
13. N. J. Jeon *et al.*, *Nat. Mater.* **13**, 897–903 (2014).
14. J.-P. Correa-Baena *et al.*, *Adv. Mater.* **28**, 5031–5037 (2016).
15. D. Forgács *et al.*, *Adv. Energy Mater.* **7**, 1602121 (2017).
16. A. Kojima, K. Teshima, Y. Shirai, T. Miyasaka, *J. Am. Chem. Soc.* **131**, 6050–6051 (2009).
17. W. S. Yang *et al.*, *Science* **348**, 1234–1237 (2015).
18. D. Bi *et al.*, *Sci. Adv.* **2**, e1501170 (2016).
19. C. Momblona *et al.*, *Energy Environ. Sci.* **9**, 3456–3463 (2016).
20. E. H. Anaraki *et al.*, *Energy Environ. Sci.* **9**, 3128–3134 (2016).
21. M. Saliba *et al.*, *Science* **354**, 206–209 (2016).
22. H. Tan *et al.*, *Science* **355**, 722–726 (2017).
23. S. S. Shin *et al.*, *Science* **356**, 167–171 (2017).
24. M. Stolterfoht *et al.*, *Energy Environ. Sci.* **10**, 1530–1539 (2017).
25. W. S. Yang *et al.*, *Science* **356**, 1376–1379 (2017).
26. K. A. Bush *et al.*, *Nat. Energy* **2**, 17009 (2017).
27. J.-P. Correa-Baena *et al.*, *Energy Environ. Sci.* **10**, 1207–1212 (2017).
28. W. Tress, *Adv. Energy Mater.* **7**, 1602358 (2017).
29. X. Li *et al.*, *Science* **353**, 58–62 (2016).
30. M. Hirasawa, T. Ishihara, T. Goto, K. Uchida, N. Miura, *Physica B* **201**, 427–430 (1994).
31. S. D. Stranks *et al.*, *Science* **342**, 341–344 (2013).
32. G. Xing *et al.*, *Science* **342**, 344–347 (2013).
33. Q. Wang *et al.*, *Appl. Phys. Lett.* **105**, 163508 (2014).
34. J. Emara *et al.*, *Adv. Mater.* **28**, 553–559 (2016).
35. H. J. Snaith *et al.*, *J. Phys. Chem. Lett.* **5**, 1511–1515 (2014).
36. E. L. Unger *et al.*, *Energy Environ. Sci.* **7**, 3690–3698 (2014).
37. W. Tress *et al.*, *Energy Environ. Sci.* **8**, 995–1004 (2015).
38. W. Tress, *J. Phys. Chem. Lett.* **8**, 3106–3114 (2017).
39. W. Tress *et al.*, *Adv. Energy Mater.* **5**, 1400812 (2015).
40. D. W. deQuilettes *et al.*, *ACS Energy Lett.* **1**, 438–444 (2016).
41. Y. Hou *et al.*, *Adv. Mater.* **28**, 5112–5120 (2016).
42. J. P. Correa Baena *et al.*, *Energy Environ. Sci.* **8**, 2928–2934 (2015).
43. M. Yang *et al.*, *Phys. Chem. Chem. Phys.* **19**, 5043–5050 (2017).
44. J. R. Poindexter *et al.*, *ACS Nano* **11**, 7101–7109 (2017).
45. W.-J. Yin, T. Shi, Y. Yan, *Appl. Phys. Lett.* **104**, 063903 (2014).
46. R. E. Brandt, V. Stevanović, D. S. Ginley, T. Buonassisi, *MRS Commun.* **5**, 265–275 (2015).
47. E. T. Hoke *et al.*, *Chem. Sci.* **6**, 613–617 (2015).
48. T. J. Jacobsson *et al.*, *Energy Environ. Sci.* **9**, 1706–1724 (2016).
49. D. P. McMeekin *et al.*, *Science* **351**, 151–155 (2016).
50. B. Conings *et al.*, *Adv. Energy Mater.* **5**, 1500477 (2015).
51. T. M. Koh *et al.*, *J. Phys. Chem. C* **118**, 16458–16462 (2014).
52. D. M. Jang *et al.*, *Nano Lett.* **15**, 5191–5199 (2015).
53. N. J. Jeon *et al.*, *Nature* **517**, 476–480 (2015).
54. N. Pellet *et al.*, *Angew. Chem. Int. Ed.* **53**, 3151–3157 (2014).
55. Z. Li *et al.*, *Chem. Mater.* **28**, 284–292 (2016).
56. C. Yi *et al.*, *Energy Environ. Sci.* **9**, 656–662 (2016).
57. T. Duong *et al.*, *Adv. Energy Mater.* **7**, 1700228 (2017).
58. D. Zhao *et al.*, *Nat. Energy* **2**, 17018 (2017).
59. V. M. Goldschmidt, *Naturwissenschaften* **14**, 477–485 (1926).
60. D. Bi *et al.*, *Nat. Energy* **1**, 16142 (2016).
61. M. Saliba *et al.*, *Energy Environ. Sci.* **9**, 1989–1997 (2016).
62. T. Matsui, J.-Y. Seo, M. Saliba, S. M. Zakeeruddin, M. Grätzel, *Adv. Mater.* **29**, 1606258 (2017).
63. B. Conings *et al.*, *Adv. Mater.* **28**, 10701–10709 (2016).
64. J. K. Nam *et al.*, *Nano Lett.* **17**, 2028–2033 (2017).
65. M. Abdi-Jalebi *et al.*, *Adv. Energy Mater.* **6**, 1502472 (2016).
66. H. Tsai *et al.*, *Nature* **536**, 312–316 (2016).
67. J. C. Blancon *et al.*, *Science* **355**, 1288–1292 (2017).
68. A. Abate *et al.*, *Energy Environ. Sci.* **8**, 2946–2953 (2015).
69. K. Domanski *et al.*, *ACS Nano* **10**, 6306–6314 (2016).
70. K. A. Bush *et al.*, *Adv. Mater.* **28**, 3937–3943 (2016).
71. A. Mei *et al.*, *Science* **345**, 295–298 (2014).
72. S. Gholipour *et al.*, *Adv. Energy Mater.* **6**, 1601116 (2016).
73. K. Aitola *et al.*, *Adv. Mater.* **29**, 1606398 (2017).
74. Z. Li *et al.*, *Energy Environ. Sci.* **10**, 1234–1242 (2017).
75. T. Leijtens *et al.*, *Nat. Commun.* **4**, 2885 (2013).
76. B. Roose *et al.*, *Nano Energy* **30**, 517–522 (2016).
77. F. Bella *et al.*, *Science* **354**, 203–206 (2016).
78. K. Domanski *et al.*, *Energy Environ. Sci.* **10**, 604–613 (2017).
79. M. Bag *et al.*, *J. Am. Chem. Soc.* **137**, 13130–13137 (2015).
80. Z. Guo *et al.*, *Science* **356**, 59–62 (2017).
81. W. Liao *et al.*, *J. Am. Chem. Soc.* **138**, 12360–12363 (2016).
82. N. K. Noel *et al.*, *Energy Environ. Sci.* **7**, 3061–3068 (2014).
83. M. A. Green *et al.*, *Prog. Photovolt. Res. Appl.* **25**, 3–13 (2017).

ACKNOWLEDGMENTS

Supported by a U.S. Department of Energy Postdoctoral Research Award, NSF grant CBET-1605495, and Skoltech 1913/R (J.-P.C.-B. and T.B.); the co-funded Marie Skłodowska Curie fellowship, H2020 grant agreement no. 665667 (M.S.); and the European Union's Horizon 2020 research and innovation program under grant agreement no. 687008 (GOTSolar) (M.G. and M.S.). The authors declare no competing financial interests. We thank T. Sargent, H. Tan, M. McGehee, K. Bush, S. S. Shin, C. Wolff, and D. Neher for providing some of the raw data presented in Fig. 4.

SUPPLEMENTARY MATERIALS

www.sciencemag.org/content/358/6364/739/suppl/DC1
Materials and Methods
Reference (*84*)

10.1126/science.aam6323

Promises and challenges of perovskite solar cells

Juan-Pablo Correa-Baena, Michael Saliba, Tonio Buonassisi, Michael Grätzel, Antonio Abate, Wolfgang Tress and Anders Hagfeldt

Science **358** (6364), 739-744.
DOI: 10.1126/science.aam6323